HHS Public Access

Author manuscript

Magn Reson Med. Author manuscript; available in PMC 2023 March 01.

Published in final edited form as:

Magn Reson Med. 2022 March ; 87(3): 1136–1149. doi:10.1002/mrm.29049.

Dynamic ^{13}C MR spectroscopy as an alternative to imaging for assessing cerebral metabolism using hyperpolarized pyruvate in humans

Junjie Ma, B.S.[a], **Marco C. Pinho, M.D.**[a,b], **Crystal E. Harrison, Ph.D.**[a], **Jun Chen, Ph.D.**[a], **Chenhao Sun, M.S.**[c], **Edward P. Hackett, M.S.**[a], **Jeff Liticker, Pharm.D.**[a], **James Ratnakar, Ph.D.**[a], **Galen D. Reed, Ph.D.**[d], **Albert P. Chen, Ph.D.**[d], **A. Dean Sherry, Ph.D.**[a,e], **Craig R. Malloy, M.D.**[a,b,f], **Steven M. Wright, Ph.D.**[c], **Christopher J. Madden, M.D.**[g], **Jae Mo Park, Ph.D.**[a,b,h,*]

[a.]Advanced Imaging Research Center, University of Texas Southwestern Medical Center, Dallas, TX, USA

[b.]Department of Radiology, University of Texas Southwestern Medical Center, Dallas, TX, USA

[c.]Department of Electrical and Computer Engineering, Texas A & M, College Station, TX, USA

[d.]GE Healthcare, Dallas, TX, USA

[e.]Department of Biochemistry and Chemical Biology, University of Texas Dallas, Richardson, TX, USA

[f.]Department of Internal Medicine, University of Texas Southwestern Medical Center, Dallas, TX, USA

[g.]Department of Neurological Surgery, University of Texas Southwestern Medical Center, Dallas, TX, USA

[h.]Department of Electrical and Computer Engineering, University of Texas Dallas, Richardson, TX, USA

Abstract

Purpose: This study is to investigate time-resolved ^{13}C MR spectroscopy as an alternative to imaging for assessing pyruvate metabolism using hyperpolarized [1-^{13}C]pyruvate in the human brain.

Methods: Time-resolved ^{13}C spectra were acquired from four axial brain slices of healthy human participants (n=4) after a bolus injection of hyperpolarized [1-^{13}C]pyruvate. ^{13}C MR spectroscopy with low flip-angle excitations and a multichannel ^{13}C/^{1}H dual-frequency RF coil were exploited

[*]**Correspondence** to: Jae Mo Park, Ph.D., 5323 Harry Hines Blvd. Dallas, Texas 75390-8568, jaemo.park@utsouthwestern.edu, Tel: +1-214-645-7206, Fax: +1-214-645-2744.

Author Contribution

M.C.P., C.J.M., J.M.P. established the study protocol; J.M., S.P., J.M.P. acquired the MR data; C.E.H., J.C., J.L., J.R., G.D.R., C.R.M. were responsible for operating the polarizer; J.M., C.S., G.D.R., A.P.C., S.M.W., J.M.P. evaluated the RF coil performance and the safety; J.M., M.C.P., J.C., J.M.P. analyzed the data; J.M.P. wrote the manuscript; All authors reviewed and approved the manuscript.

Conflict of Interest

G.D.R. and A.P.C. are employees of GE Healthcare.

for reliable and unperturbed assessment of hyperpolarized pyruvate metabolism. Slice-wise area under the curves (AUCs) of ^{13}C-metabolites were measured and kinetic analysis was performed to estimate the production rates of lactate and HCO_3^-. Linear regression analysis between brain volumes and hyperpolarized signals was performed. Region-focused pyruvate metabolism was estimated using coil-wise ^{13}C reconstruction. Reproducibility of hyperpolarized pyruvate exams was presented by performing two consecutive injections with a 45-min interval.

Results: [1-^{13}C]Lactate relative to the total ^{13}C signal (tC) was 0.21–0.24 in all slices. [^{13}C]HCO_3^-/tC was 0.065–0.091. Apparent conversion rate constants from pyruvate to lactate and HCO_3^- were calculated as 0.014–0.018s^{-1} and 0.0043–0.0056s^{-1}, respectively. Pyruvate/tC and lactate/tC were in moderate linear relationships with fractional grey matter volume within each slice. White matter presented poor linear regression fit with hyperpolarized signals, and moderate correlations of the fractional cerebrospinal fluid volume with pyruvate/tC and lactate/tC were measured. Measured hyperpolarized signals were comparable between two consecutive exams with hyperpolarized [1-^{13}C]pyruvate.

Conclusions: Dynamic MRS in combination with multichannel RF coils is an affordable and reliable alternative to imaging methods in investigating cerebral metabolism using hyperpolarized [1-^{13}C]pyruvate.

Keywords

human brain; dynamic nuclear polarization; magnetic resonance spectroscopy; hyperpolarized pyruvate; reproducibility

INTRODUCTION

In vivo brain metabolism and function have been widely investigated using functional MRI, positron emission tomography (PET), and ^{1}H MR spectroscopy (MRS). These conventional imaging methods, however, have limited access to *in vivo* metabolism (1–3). ^{13}C NMR methods with steady-state infusion of a ^{13}C-labeled substrate can provide detailed metabolic utilization of the substrate, but the signal-to-noise ratio (SNR) is inherently poor due to the low gyromagnetic ratio (4). In 2003, the dissolution dynamic nuclear polarization (DNP) technique in combination with ^{13}C MR spectroscopic imaging (MRSI) was introduced as a new imaging modality that can assess the real-time utilization of substrates and formation of downstream products *in vivo* by boosting the SNR (5). Unlike PET, specific metabolic pathways may be monitored, and the products are distinguishable from the injected substrate using this technique. Moreover, ^{13}C is a non-radioactive stable isotope, potentially safe to perform multiple consecutive investigations.

Due to its pivotal role in carbohydrate metabolism and the molecular characteristics ideally suited for the dissolution DNP, [1-^{13}C]-labeled pyruvate was the first developed substrate for *in vivo* studies (6) with dominant applications in cancer (7) and cardiac metabolism (8). Intravenously injected hyperpolarized (HP) [1-^{13}C]pyruvate can be transported to the intracellular space via monocarboxylate transporters (MCTs), generating [1-^{13}C]lactate and [1-^{13}C]alanine in the cytoplasm via lactate dehydrogenase (LDH) and alanine aminotransferase (ALT), respectively, or acetyl-CoA + [^{13}C]CO_2, which is typically detected

as bicarbonate ([^{13}C]HCO_3^-), via pyruvate dehydrogenase (PDH) in the mitochondria. In the brain, changes in HP [1-^{13}C]lactate production have been featured as surrogate biomarkers for pathological processes such as glioblastoma (9), neuroinflammation (10), and traumatic brain injury (TBI) (11). [^{13}C]HCO_3^- production was reported in the cortex of rat brains (12), providing a complementary biomarker for cerebral PDH activity or mitochondrial integrity (11,13). Alanine production in the brain is reportedly negligible (12) due to the low ALT activity (14).

Recent advances in clinical translation of HP pyruvate imaging (15) has enabled metabolic imaging of the human brain in healthy subjects (16,17) and patients with brain tumors (17–20) or TBI (21). Most previous human brain studies focused on imaging altered lactate production in intracranial malignancies (18,19). Despite the unprecedently high sensitivity of HP signals, accurate and reliable imaging of pyruvate metabolism in the brain is still challenging. To establish an appropriate brain imaging strategy, reliable assessment of HP pyruvate and products in the brain and their dynamic behaviors are essential. In particular, production of [^{13}C]HCO_3^-, a salient surrogate biomarker of *in vivo* PDH activity and, potentially, mitochondrial integrity, is much smaller than the other major cerebral product, [1-^{13}C]lactate. Indeed, previous studies reported inconsistent measurement of [^{13}C]HCO_3^-, ranging from less than 2% (22) to 8% (16) relative to the [1-^{13}C]pyruvate signals. Another study described the [^{13}C]HCO_3^- SNR being ‘greatly variable’ (23). As kinetic analysis of time-resolved HP signals demands higher SNRs than time-averaged analysis, the apparent conversion rates (*k*’s) from pyruvate to products reported in the previous studies have larger discrepancies (16,23).

Non-imaging approaches using MRS provide excellent signal sensitivities, leading to more robust measurements of HP products and the kinetics. Due to the superior SNR, a small flip-angle RF excitation suffices for reliable [^{13}C]HCO_3^- assessment, allowing frugal utilization of HP magnetization, and thus, enables either longer observations or improved temporal resolution. Although MRS data of HP [1-^{13}C]pyruvate for human brain were shown previously (16,18), the analysis was brief with limited number of subjects, and the studies were either performed with a suboptimal RF coil for brain (18) or analyzed in poorly resolved peaks in the spectrum (16).

In this study, we report reliable measurements and analysis of HP [1-^{13}C]pyruvate and its products, [1-^{13}C]lactate and [^{13}C]HCO_3^-, in the brain using time-resolved ^{13}C MRS from healthy volunteers. Here, we demonstrate the potential of assessing spatial information using multi-slice acquisition and ^{13}C RF receive arrays. Moreover, repeatability and reproducibility of HP [1-^{13}C]pyruvate for brain studies are evaluated by performing consecutive injections of HP pyruvate.

METHODS

MR scanner and RF coils

All MR studies were performed using a 70-cm wide-bore 3T 750w Discovery™ MR scanner (GE Healthcare, Waukesha, Wisconsin, USA). A ^{13}C/^{1}H dual-frequency RF head coil that consists of ^{1}H quadrature transmit (Tx) and receive (Rx), ^{13}C quadrature Tx and 8-channel

^{13}C Rx arrays (Clinical MR Solutions, LLC, Brookfield WI, USA) was developed for the study. A rigid nested design was utilized for the ^{1}H coil (⊘ [diameter] = 30.4 cm, length = 30.5 cm) and the ^{13}C Tx coil (⊘ = 26.8 cm, length = 25.4 cm). The anterior ^{13}C Rx array coils (5–8 channels) are attached to the inner surface of the ^{13}C Tx coil, and the posterior Rx array (1–4 channels) are flexible to maximize the receive sensitivity. Each coil element of the ^{13}C Rx arrays is 12.7 cm × 16.5 cm. The entire anterior portion of the head coil is detachable for head positioning (24). The structure of the head coil is shown in Figure 1. The ^{13}C coil Tx performance was tested with a gadolinium-doped spherical [^{13}C]HCO_3^- phantom (0.4 M, ⊘ = 18 cm) and a free induction decay chemical shift imaging (FID CSI) sequence (matrix size = 16 × 16, repetition time [TR] = 5 s, field of view [FOV] = 24 cm × 24 cm). Performance of the ^{13}C coils is summarized in Figure S1. The B_1^+ profile was calculated using a double-angle method, Figure S1A. Receive performance was separately tested using a cylindrical phantom (⊘ = 14 cm) that contains non-labeled pure ethylene glycol (natural abundance 1.1% of ^{13}C) to avoid partial volume effects along the slice encoding direction due to the phantom shape, Figure S1B. At the center of the cylindrical phantom, the coil sensitivity was 78% of the phantom. The cross-sectional signal changes demonstrate the reliable and relatively homogeneous signal detection from the entire phantom when all the coil elements are combined, and region-focused detections from individual coils. The safety of the coil was tested by simulation, phantoms, and approved by the Advanced Imaging Research Center.

SNR comparison between MRS and MRI in a phantom

To demonstrate the SNR advantage of a small flip-angle MRS over MRI with full RF excitation, a simple phantom test was performed using the spherical [^{13}C]HCO_3^- phantom and the ^{13}C/^{1}H head coil. A slice-selective single-shot spiral ^{13}C imaging (flip-angle = 90°, slice thickness [ST] = 15 mm, TR = 3 s, FOV = 24 cm × 24 cm, 128 averages) was applied to acquire 2D ^{13}C images with three different nominal in-plane spatial resolutions (3.0 cm × 3.0 cm, 1.5 cm × 1.5 cm, 1.0 cm × 1.0 cm) by adjusting the spiral readouts. From the same phantom, ^{13}C FID was also acquired using a 6.5° slice-selective excitation (ST = 15 mm, TR = 3 s, 128 averages, 1 slice, spectral bandwidth = 10000 Hz, spectral points = 4096). Peak SNRs (SNR_{peak}) were compared between the images and the magnitude spectrum.

Human subjects

Four healthy adults were recruited for the study (age: 24 – 65 years, 1 male and 3 females, body mass index = 26.4 ± 2.9, mean ± standard deviation). The participants' information is summarized in Table 1. Each participant was imaged with the brain MR protocol, which includes two injections of HP [1-^{13}C]pyruvate (IND#: 133229) and a series of ^{1}H MRI. Subject #1 received only one HP injection. A written and informed consent was obtained from all the study participants. The imaging protocol is fully compliant with the Health Insurance Portability and Accountability Act (HIPAA) regulation and was approved by the Institutional Review Board (IRB) of The University of Texas Southwestern Medical Center (IRB#: STU 072017-009, ClinicalTrials.gov ID: NCT03502967). All subjects tolerated the procedure without any incident.

Dynamic nuclear polarization (DNP) and Quality control (QC)

A clinical SPINlab™ polarizer (GE Healthcare) was used for DNP. Up to three pyruvate samples were simultaneously polarized for each subject. Each pyruvate sample was prepared by mixing 1.47 g of GMP-grade 14-M [1-^{13}C]pyruvic acid (Sigma Aldrich, St Louis, Missouri, USA) with 27.7 mg of AH111501 EPA radical (Syncom, Groningen, Netherlands). After assembly in sterile environment, clinical fluid paths were transferred to the SPINlab for polarization and compounding. The pyruvate samples were polarized for 3 – 4.5 hrs, then dissolved by 38 mL of sterile water at 130 °C. The HP pyruvate solution was mixed with 36.5 mL of room temperature TRIS/NaOH media (333 mM/600 mM) and passed a quality control (QC) analysis prior to the injection. Terminal filtering, filter integrity bubble point test, pH strip confirmation and volume check were performed in addition to the automated QC. For each ^{13}C acquisition, a bodyweight-adjusted volume (0.43 mL/kg) of 250 mM pyruvate was injected at a rate of 5 mL/s, followed by a 25-mL saline flush at the same rate. Pyruvate concentration (242.6 ± 16.2 mM, n = 7), pH (7.6 ± 0.4), polarization level (33.7 ± 6.0 %), and residual radical (0.9 ± 0.8 μM) of the injectate were measured using the QC device (GE Healthcare) immediately after each dissolution. The transfer time from dissolution to the beginning of injection was 63.1 ± 6.7 s.

MR protocol

Each subject was scanned with a fast gradient recalled echo (GRE) localizer and a 2D T_2-weighted fluid-attenuated inversion recovery (FLAIR; TR = 8 s, echo time [TE] = 144.7 ms, FOV = 24 cm × 24 cm, acquisition matrix = 256 × 256, ST = 5 mm) to localize the brain and prescribe imaging slices. Time-resolved ^{13}C spectra were acquired with an injection of HP pyruvate using a slice-selective dynamic MRS (flip-angle = 6.5°, TR = 3 s, spectral width = 10000 Hz, spectral points = 4096, scan time = 4 min, ST = 1.5 cm, 4 slices). The ^{13}C transmit power was calibrated using an independent phantom scan (the 0.4-M [^{13}C]HCO_3^- phantom). The ^{13}C frequencies were calculated from the ^{1}H water frequency of the PRESS sequence and set on [1-^{13}C]pyruvate resonance. The second ^{13}C scan with additional HP [1-^{13}C]pyruvate injection was performed 45 min after the first injection. Additional ^{1}H images such as dual echo T_2-weighted fast spin echo (FSE; TR = 5 s, TE_1/TE_2 = 10.12 ms/60.72 ms, FOV = 24 cm × 24 cm, acquisition matrix = 192 × 192, ST = 5 mm) were acquired during the 45-min time interval.

Data reconstruction and analysis

All the ^{13}C data were reconstructed in absorption mode via a custom-made reconstruction pipeline that integrates coil-wise reconstruction, phase correction (0^{th} and 1^{st} order), and coil combination. Metabolite peaks were quantified from time-averaged ^{13}C spectra. For display purpose, the baseline was subtracted from the time-averaged spectra by fitting a spline to the signal-free regions of the smoothed spectrum. Kinetic analysis was performed between pyruvate, lactate and HCO_3^- to estimate the apparent conversion rates (k_{PL}, k_{PB}) and *in-vivo* longitudinal relaxation times (T_1) using a three-site exchange model (25), which was extended from the previously described two-site exchange model (26). Due to its small relevance to cerebral metabolism, alanine signal was excluded from the kinetic analysis. The time point where the maximum of each metabolite signal was achieved ($\boldsymbol{\tau}$)

was measured to assess the pyruvate delivery time and the metabolite production rate. The production rate of each metabolite was also estimated from the mean slope of the first three time points (r) following its appearance in the dynamic curve by linearly fitting the metabolite signal, which was then normalized to the initial mean slope of pyruvate (27–29). Both metabolite ratios and the kinetic analysis are independent of polarization level at the time of injection. For non-ratio metabolite peak assessment, each HP ^{13}C data was divided by the following coefficient to compensate for the experimental variability in polarization performance and transfer time from the dissolution until the injection to the subject. *In vitro* T_1 of [1-^{13}C]pyruvate was estimated as 78 s.

$$\frac{[pyruvate]_{QC}}{250} \bullet \frac{polarization_{QC}}{100} \bullet e^{-\frac{T_{transfer}}{T_{1,\ pyruvate}}}$$

Brain segmentation

Brain extraction and segmentation for ^{1}H human brain image was conducted using FSL package (FMRIB, Oxford, UK) (30,31). Firstly, a binary brain mask was generated from multi-slice ^{1}H T_2-weighted images, which was used to extract brain tissue from corresponding ^{1}H T_1-weighted images. Secondly, the skull-stripped multi-slice ^{1}H T_1-weighted images were fed into FSL for brain segmentation, generating multi-slice possibility maps for GM, WM and CSF. Finally, with the original skull-stripped ^{1}H T_1-weighted images and the possibility maps, multiple-slice information was combined to calculate single-slice possibility maps of GM, WM and CSF that match the imaged ^{13}C slice.

Statistical analysis

Data are presented as mean ± standard deviation. Statistical significance in metabolite ratios between brain regions was evaluated from the study participants collectively by a paired t-test ($\alpha = 0.05$, two-tailed). Reproducibility of HP pyruvate (1st and 2nd injections) was tested using one-way ANOVA ($\alpha = 0.05$). Least square fitting was used for linear regression between brain volumes and HP signals, and Pearson product-moment correlation coefficient (r) was calculated to measure the linear relationship. Coefficient of determination (R^2) was calculated to estimate the goodness of fit, and the statistical significance was evaluated by t-statistics (two-tailed) with a reduced degree of freedom to reflect the dependency between brain slices acquired from the same subject.

RESULTS

(R1–1) In the phantom study, shown in Figure 2, the HCO_3^- SNR_{peak} in the ^{13}C spectrum, acquired using MRS with 6.5° flip-angle was compared with SNR_{peak} of ^{13}C images that were acquired with 90° excitations. SNR_{peak} from the MRS spectrum was 4.6×, 5.8× and 7.0× higher than SNR_{peak} of ^{13}C images with 3 cm, 1.5 cm, and 1 cm of nominal spatial resolution, respectively.

In human studies, carbon spectra of four 15-mm thick axial brain slices were acquired using a small flip-angle RF excitation every 3s. The most inferior slice (slice #1) was prescribed to include the ganglia and corpus callosum, and slice #2 was prescribed to include the body of the lateral ventricles. Slices #3 and #4 include cingulate gyrus valley and frontoparietal cortex, respectively. Time-averaged spectra of slice #1 – 4 from a representative participant are shown in Figure 3A. Besides [1-^{13}C]pyruvate (171.3 ppm) and [1-^{13}C]pyruvate-hydrate (179.7 ppm), metabolic products such as [1-^{13}C]lactate (183.6 ppm), [1-^{13}C]alanine (177.0 ppm) and [^{13}C]HCO_3^- (161.3 ppm) were detected. No products specific to pyruvate carboxylase (PC) pathway were detected. [1-^{13}C]Lactate relative to the total HP ^{13}C signal (tC) was consistent throughout the slices, and the average lactate/tC of each slice over the participants (n = 4) ranged from 0.212 ± 0.018 to 0.244 ± 0.039. [^{13}C]HCO_3^- production was 30 – 37 % of lactate. The difference in [^{13}C]HCO_3^-/tC between the slices was not statistically significant ($p > 0.08$). [1-^{13}C]Alanine production was much smaller than lactate or HCO_3^-. Metabolite ratios of HP ^{13}C signals are summarized in Figure 3B–C and Table 2. Areas under the curves (AUCs) for [1-^{13}C]pyruvate, [1-^{13}C]lactate, and [^{13}C]HCO_3^- signals were positively correlated to the volume of grey matter (GM, $r > 0.5$, $p \leq 0.03$) within each slice. The metabolite signals were positively and negatively correlated to white matter (WM, $r > 0.4$, $p = 0.06 – 0.10$) and cerebrospinal fluid (CSF, $r < -0.4$) volumes, respectively, but not statistically significant, Figure 4A. The pyruvate signal normalized by tC maintained the positive correlation with fractional GM ($r = 0.57$, $p = 0.02$) volumes and negative correlation with fractional CSF volume ($r = -0.64$, $p = 0.008$), Figure 4B. However, lactate/tC showed a strong negative correlation with fractional GM volume ($r = -0.54$, $p = 0.03$) and a positive correlation with fractional CSF volume ($r = 0.54$, $p = 0.03$). Pearson's correlation coefficients, coefficients of determination, and p-values for the linear regression between the brain tissue volumes and HP signals are summarized in Table S1, S2, and S3, respectively.

Region-weighted assessment was performed by coil-by-coil reconstruction. ^{13}C Rx coil elements that are positioned near the temporal lobes detected larger [1-^{13}C]lactate/tC measurements (0.197 ± 0.018 from coils 1 and 4, 0.190 ± 0.016 from coils 5 and 8) than frontal lobe (0.183 ± 0.018 from coils 6 and 7, $p < 0.01$). [^{13}C]HCO_3^-/tC from the temporal lobes (0.062 ± 0.006 for coils 1 and 4, 0.059 ± 0.003 for coils 5 and 8) were also larger than the metabolic signals in the frontal lobe (0.049 ± 0.007 for coils 6 and 7) but smaller than those in the occipital lobe (0.072 ± 0.007 from coils 2 and 3, $p < 0.05$). As shown in Figure 5, region-weighted [1-^{13}C]lactate/tC and [^{13}C]HCO_3^-/tC could be generated from coil-wise assessment of the metabolites in the time-averaged spectra of individual coil elements.

Dynamic behavior of HP signals was described by initial slopes ($\boldsymbol{s}$) and times-to-peak ($\boldsymbol{\tau}$) for each metabolite (Fig.6A). Initial slopes for lactate ($\boldsymbol{s}_{lac}$) and HCO_3^- ($\boldsymbol{s}_{bic}$) normalized by the pyruvate slope ($\boldsymbol{s}_{pyr}$) were 0.055 ± 0.005 ($\boldsymbol{s}_{lac}/\boldsymbol{s}_{pyr} = \boldsymbol{r}_{lac}$, n = 4) and 0.014 ± 0.004 ($\boldsymbol{s}_{bic}/\boldsymbol{s}_{pyr} = \boldsymbol{r}_{bic}$), respectively, for slice #1 and similar for the other slices ($\boldsymbol{r}_{lac} = 0.056 – 0.064$, and $\boldsymbol{r}_{bic} = 0.014 – 0.017$, Fig.6C). Time-to-peak of [1-^{13}C]lactate ($\boldsymbol{\tau}_{\mathrm{lac}}$) and [^{13}C]$HCO_3^-$ ($\boldsymbol{\tau}_{\mathrm{bic}}$) was 8.3 ± 2.9 s and 12.8 ± 2.9 s longer than that of [1-^{13}C]pyruvate ($\boldsymbol{\tau}_{\mathrm{pyr}}$) for slice #1. The difference in time-to-peak between metabolites was similar for the other slices ($\boldsymbol{\tau}_{\mathrm{lac}} - \boldsymbol{\tau}_{\mathrm{pyr}} = 8.3 – 9.0$ s, $\boldsymbol{\tau}_{\mathrm{bic}} - \boldsymbol{\tau}_{\mathrm{pyr}} = 12.8 – 13.5$ s, Fig.6D). The apparent conversion rate constants from pyruvate to

lactate (k_{PL}) and HCO_3^- (k_{PB}) were calculated as 0.0140 ± 0.0011 s^{-1} and 0.0043 ± 0.0005 s^{-1} (slice #1), respectively, by fitting the measured timecurves to a multi-site exchange model (Fig.6B). The k_{PL} ranged from 0.0151 to 0.0176 s^{-1} and k_{PB} was 0.0045 – 0.0056 s^{-1} for the other slices (Fig.6E). *In vivo* T_1 of lactate and HCO_3^- were estimated as 24.0 ± 0.7 s and 25.5 ± 0.6 s, respectively. Temporal changes in metabolite ratios for lactate and HCO_3^- were investigated from 21 to 78 s, where the HCO_3^- measurement was reliable. Both lactate/tC and HCO_3^-/tC increased over time and reflected the initial cardiac cycle (Fig.7A–B) whereas HCO_3^--to-lactate ratio monotonically increased in a logarithmic shape (Fig.7C).

AUCs of HP metabolite relative to tC were comparable between data acquired from two consecutive HP [1-^{13}C]pyruvate injections with an interval of 45 minutes between the injections (Fig.8A, n = 12, p = 0.05 for lactate/tC, p = 0.1 for alanine/tC, p = 0.5 for HCO_3^-/tC, p = 0.2 for pyruvate/tC). Difference in times-to-peak ($\boldsymbol{\tau}$) and relative initial slopes ($\boldsymbol{r}$) was also not significant between injections (Fig.8B, p > 0.3). No significant difference was observed in apparent conversion rate constants (Fig.8C, p = 0.5 for k_{PL}, p = 0.1 for k_{PB}).

DISCUSSION

Unlike conventional MR methods, studies with HP ^{13}C substrates rely on exogenously administered MR signal sources, which are non-recoverable after RF excitations and rapidly decay over time. Due to the disposability and the transience of HP signals, the continuous replenishment of the injected HP substrates via the blood circulation, and the complex metabolic reactions, quantitative analysis of HP metabolism is not trivial. Acquisition parameters such as flip-angle, sampling period, and k-space readout trajectory can also affect the quantification of HP metabolites significantly. Moreover, performance of the RF coil impacts the signal sensitivity and detection coverages, another key factor that needs to be considered in data analysis. The large discrepancies of the reported metabolite ratios and kinetic parameters in recent translational studies of HP pyruvate to human brains are largely due to the inconsistencies in acquisition scheme, coil sensitivity, and SNR in addition to inter-subject variability. While imaging approaches measure reliable pyruvate and lactate distributions, it is technically challenging for small metabolite peaks such as HCO_3^-. Single time-point imaging omits kinetic information and, thus, is partial. An alternative approach is to acquire MR signal without spatial encoding. Although this approach does not provide spatial information, it can improve temporal resolution and achieve excellent SNR. The intent of our study was to measure the cerebral metabolism of HP [1-^{13}C]pyruvate in the human brain in a reliable and unbiased way while maintaining sufficient SNRs for key products, spatial detection coverage, and accurate brain registration. We also extended MRS analysis to take a glimpse of ^{13}C/^{1}H combined analysis and regional assessment of HP pyruvate metabolism by exploiting a dual-frequency ^{13}C/^{1}H RF coil with multichannel ^{13}C receive array.

To minimize the signal loss due to RF sampling and its impact on the multi-slice acquisition, a small flip-angle (6.5°) was used for RF excitation with a moderate 3-s sampling period. The ^{13}C quadrature Tx coil was used to provide homogeneous excitations over the brain

region. The receive profile was sufficiently large and spatially homogeneous to assess signals from deep white matter and central brain structures. Despite the small flip-angle, we could reliably observe time-resolved [1-^{13}C]lactate and [^{13}C]HCO_3^- over more than 90s, providing minimally perturbed observations of HP [1-^{13}C]pyruvate kinetics. Spectral analysis in pure absorption mode resolved all the ^{13}C peaks without cross contamination, which can interfere not only with accurate peak quantification but also kinetic analysis. For instance, a previous study that analyzed MRS in magnitude mode showed contamination of the large HP pyruvate peaks on products (16). As a result, the time-to-peak for [^{13}C]HCO_3^- was aligned with that for [1-^{13}C]pyruvate. In our study, HCO_3^- was peaked approximately 13 s after pyruvate peaked.

In the present study, kinetic analysis was performed using two largely acceptable methods. The first analysis describes the production rate of each metabolite, based on its initial appearance using the time-to-peak (**τ**) and the initial slopes (**s**). The second analysis estimates the apparent metabolite conversion rate constants (k) and *in vivo* T_1s. Compared to the previous brain studies (16,23), the inter-subject variability of the parameters was much smaller. This could be due to the lack of spatial selectivity of simple slice-selective MRS, blurring region-specific inter-subject variability, but is also possibly due to high SNRs. The time-resolved measurements and the AUCs of HP [1-^{13}C]pyruvate, [1-^{13}C]lactate and [^{13}C]HCO_3^- reported in this study will provide useful and reliable reference for future studies in developing MR acquisition strategies and interpreting imaging results. For instance, metabolite ratios are commonly used to describe radiographic analysis of HP results even for single time-point images. Although reliability of HCO_3^-/lactate attenuates in the later time points due to the decreasing SNRs of the HP signals, our data showed that the HCO_3^--to-lactate ratio rapidly and monotonically increases over time from less than 0.2 at 20 s to more than 0.5 at 80 s in all imaging slices (Fig.7C), implying that the single-time-point approach needs to be performed and interpreted carefully. Moreover, this study showed that the kinetic profile of pyruvate-hydrate, a pH-regulated and metabolically inactive product, was similar to that of pyruvate (Fig.6A). The constant ratio between pyruvate-hydrate and pyruvate over time (Fig.7D) confirms the inertness of pyruvate-hydrate.

Quantification of HP signals, acquired from slice-selective MRS, should be performed in the context of constituent tissue elements within the slice. The fractional amount of each tissue type and its metabolic characteristics as well as microstructural information such as perfusion or cellular density needs to be understood to properly interpret the acquired HP signals. As part of this approach, tissue regression analysis was performed by comparing HP signals with segmented ^{1}H MRI of the corresponding brain slice to interrogate lactate and HCO_3^- production in GM, WM, and CSF. In principle, the kinetics of HP pyruvate metabolism are a function of pyruvate delivery to the brain, LDH activity and PDH activity. The transport of pyruvate through the blood–brain barrier (BBB) consists of both a saturable MCT-facilitated process and a passive diffusion process. MCT1 is mainly detected on endothelial cells of the BBB (32,33) and has been reported as a rate limiting step for the conversion of HP pyruvate to lactate (34,35) and HCO_3^- (36) in the brain. Previous studies also suggested that BBB transport is saturated with a bolus injection of HP pyruvate (37,38). MCT transportation to astrocytes and neurons is not likely further limited as they

express sufficient MCT2 and MCT4 (Km = 3.5 – 28 mM) (32,39). We correlated GM, WM, and CSF volumes with HP signals because the tissue compartments have distinctive characteristics in perfusion, MCT, enzyme activities, and intrinsic metabolite pool sizes (39–43). Measured HP signals of pyruvate, lactate, and HCO_3^- within the prescribed brain slices were largely proportional to GM and WM volumes within the slice. The strong positive correlation of the detected HP pyruvate and lactate signals with the total GM volumes as well as the positive relationship between tC-normalized HP pyruvate and fractional GM suggest that GM is likely the dominant tissue types that produce HP signals. The positive correlation between the GM volume and HP signals were reported previously (16,22) and are supported by 1.4–4 times higher perfusion in GM than WM (40). Moreover, the MCT family transports pyruvate and lactate into cells more rapidly in GM (pKm = 1 mM) than in WM (pKm = 0.1 mM) (39). GM has nearly twice high LDH expression as WM (41). However, the positive correlation of HP signals with WM volumes does not necessarily indicate that the HP signals are proportional to WM volumes. Indeed, the fractional HP lactate and HCO_3^- amounts decreased as the fractional WM increased. This could be due to normalization by pyruvate-dominant tC or saturated transport to brain cells via the BBB. HP pyruvate signal decreased as the CSF volume increased for both total or fractional quantification, which may be due to the low perfusion. CSF was the only site where fractional HP lactate was positively correlated with fractional volume. Despite the lower LDH expression in CSF than in GM and WM (41), the significantly larger lactate pool size in CSF (1.2–2.1 mM) (42) than in WM and GM (0.6–1 mM (43)) probably contributed to the positive correlation between lactate/tC and the fractional CSF.

The neurovascular coupling of astrocytes (44), the large contribution of lactate conversion in plasma and other organs (45,46), and rapid lactate shuttle between astrocytes and neurons suggest that both neurons and astrocytes as well as vasculature and extracellular space contribute to HP lactate signal. In mitochondria, pyruvate is largely metabolized via PDH or PC, which are dominant in neurons and astrocytes, respectively (44,47,48). Previously, production of ^{13}C-labeled aspartate, malate, and fumarate from HP [1-^{13}C]pyruvate was suggested as surrogate biomarkers for pyruvate carboxylation (49). [^{13}C]HCO_3^- can be produced from HP [1-^{13}C]pyruvate via both PDH and PC pathways (25,50). Since neuronal pyruvate carboxylation does not play an important quantitative role (51,52), the absence of PC-specific HP products in the brain implies that the HCO_3^- was primarily generated via PDH flux in neurons. This result is supported by the large cortical HP HCO_3^- production in previous imaging studies (12,22) and suggests that HP [1-^{13}C]pyruvate is preferably metabolized in neurons and, therefore, probes neuron-specific metabolism. Other metabolic pathways such as ALT and aspartate aminotransferase that are tightly associated with pyruvate carboxylation (53) are also unlikely detectable in the brain *in vivo* using HP pyruvate.

Assessment of cerebral alanine production would provide unique opportunity to estimate alanine cycling, an important metabolic step for transferring ammonia, which is essential in the glutamate/glutamine cycling, to glial cells. However, we excluded alanine from the analysis because the dominant source of alanine production is likely peripheral muscle tissue rather than the brain as previously reported (12,54). Indeed, the peak shape of the detected

alanine peak was highly variable and dissimilar to the other peaks, reflecting that the alanine distribution was different from the other ^{13}C-metabolites.

In vivo investigation of HP pyruvate using dynamic MRS has several advantages over imaging approaches. First, the method is technically affordable. The simple FID acquisition does not need demanding hardware requirements (e.g., gradient performance). Moreover, the spectroscopic acquisition is less prone to artifacts. For instance, spectral spatial RF excitation with imaging readouts (17,22) or imaging with different echo times and IDEAL (iterative decomposition of water and fat with echo asymmetry and least-squares estimation) reconstruction (16) that were utilized in the previous human brain studies are susceptible to potential signal contamination of the large pyruvate signal due to B_0 inhomogeneity and sideband RF excitations. Second, the achievable SNR is higher than imaging methods at the expense of spatial information. Therefore, it is worth it to consider dynamic MRS for assessment of metabolites with SNR challenges. Indeed, a limited number of studies reported cerebral [^{13}C]HCO_3^- maps with compromised SNR. With dynamic MRS, HCO_3^- kinetics could be acquired with adequate SNR even with 6.5° excitation, allowing nearly unperturbed full observation of *in vivo* HP pyruvate to HCO_3^- conversion. If needed, SNR can be further improved by simply increasing the flip-angle. As a non-imaging method, MRS has limited access to spatial information. However, regional assessment of lactate/tC and HCO_3^-/tC was attempted by exploiting the multichannel receive array and multi-slice acquisition. The coil-wise spectral analysis could quantify HP metabolites populated in the immediate vicinity from each ^{13}C receive coil element. Acknowledging the cerebral cortices as dominant HP signal sources (55), the coil-by-coil analysis has potential for assessing regional brain metabolism. In particular, the coil-wise analysis is more appropriate for RF coils with a larger number of receive arrays with a smaller dimension of each coil element. Moreover, identification of coil locations and correction of multichannel sensitivity will be required for more systematic and accurate regional assessment of each metabolite (as opposed to metabolite ratios as demonstrated in this study) (56).

Because of the absence of radioactivity, serial injections of HP pyruvate are acceptable. The repeatability of HP pyruvate exams was briefly discussed in a previous cardiac study (57), but no prior human study has reported the reproducibility of HP measurements in the brain. We demonstrated the feasibility of two consecutive injections of HP pyruvate with a 45-minute time-interval between the injections and did not detect any noticeable difference in the acquired dynamic ^{13}C spectra between the injections. This study, therefore, lays the groundwork for longitudinal studies such as monitoring the acute response to a therapy following the baseline scan in a single MR session. However, considering the small number of participants in this study and multiple potential physiological variables, further studies with a larger group will be needed to verify the reproducibility or to investigate subtle changes in metabolism due to the first injection of HP pyruvate.

The rate of oxidative metabolism and biosynthetic processes in the brain is high. Altered utilization of glucose and other substrates such as lactate or ketones occurs in different nutritional states or in several neurological disorders. As demonstrated in preclinical studies, HP [1-^{13}C]pyruvate has potential in imaging metabolic alterations which commonly manifest in neurological pathological states, including intracranial malignancies,

neuroinflammation, and brain injuries. Hosever, several neuropathological conditions are often associated with additional technical challenges, such as decreased HCO_3^- production and magnetic susceptibility secondary to hemorrhage or calcifications. Dynamic ^{13}C MRS in combination with multichannel RF coils would be as an affordable and reliable alternative to imaging methods in investigating cerebral metabolism using HP [1-^{13}C]pyruvate.

Supplementary Material

Refer to Web version on PubMed Central for supplementary material.

Acknowledgements

Funding:

The Mobility Foundation; The Texas Institute for Brain Injury and Repair; National Institutes of Health of the United States (R01 NS107409, P41 EB015908, S10 OD018468, S10 RR029119); The Welch Foundation (I-2009-20190330); UT Dallas Collaborative Biomedical Research Award (UTD 1907789). We thank Ralph S. Hashoian for building the RF head coil.

Personnel Support:

The authors appreciate Jeannie Baxter, Lucy Christie, Kelley Derner, Maida Tai and Salvador Pena for recruiting and imaging the volunteers.

References

1. Hall CN, Howarth C, Kurth-Nelson Z, Mishra A. Interpreting BOLD: towards a dialogue between cognitive and cellular neuroscience. Philos. Trans. R. Soc. Lond., B, Biol. Sci 2016;371:20150348. doi: 10.1098/rstb.2015.0348. [PubMed: 27574302]
2. Salmon E, Bernard Ir C, Hustinx R. Pitfalls and Limitations of PET/CT in Brain Imaging. Semin Nucl Med 2015;45:541–551. doi: 10.1053/j.semnuclmed.2015.03.008. [PubMed: 26522395]
3. Zhu H, Barker PB. MR spectroscopy and spectroscopic imaging of the brain. Methods Mol. Biol 2011;711:203–226. doi: 10.1007/978-1-61737-992-5_9. [PubMed: 21279603]
4. Cheshkov S, Dimitrov IE, Jakkamsetti V, Good L, Kelly D, Rajasekaran K, DeBerardinis RJ, Pascual JM, Sherry AD, Malloy CR. Oxidation of [U-13 C]glucose in the human brain at 7T under steady state conditions. Magn Reson Med 2017;78:2065–2071. doi: 10.1002/mrm.26603. [PubMed: 28112825]
5. Ardenkjaer-Larsen JH, Fridlund B, Gram A, Hansson G, Hansson L, Lerche MH, Servin R, Thaning M, Golman K. Increase in signal-to-noise ratio of > 10,000 times in liquid-state NMR. Proc. Natl. Acad. Sci. U.S.A 2003;100:10158–10163. doi: 10.1073/pnas.1733835100. [PubMed: 12930897]
6. Golman K, in 't Zandt R, Thaning M. Real-time metabolic imaging. Proc Natl Acad Sci USA 2006;103:11270–11275. doi: 10.1073/pnas.0601319103. [PubMed: 16837573]
7. Brindle KM, Bohndiek SE, Gallagher FA, Kettunen MI. Tumor imaging using hyperpolarized 13C magnetic resonance spectroscopy. Magn Reson Med 2011;66:505–519. doi: 10.1002/mrm.22999. [PubMed: 21661043]
8. Rider OJ, Tyler DJ. Clinical implications of cardiac hyperpolarized magnetic resonance imaging. J Cardiovasc Magn Reson 2013;15:93. doi: 10.1186/1532-429X-15-93. [PubMed: 24103786]
9. Park I, Larson PEZ, Zierhut ML, et al. Hyperpolarized 13C magnetic resonance metabolic imaging: application to brain tumors. Neuro-oncology 2010;12:133–144. doi: 10.1093/neuonc/nop043. [PubMed: 20150380]
10. Guglielmetti C, Najac C, Didonna A, Van der Linden A, Ronen SM, Chaumeil MM. Hyperpolarized 13C MR metabolic imaging can detect neuroinflammation in vivo in a multiple sclerosis murine model. Proc Natl Acad Sci USA 2017;114:E6982–E6991. doi: 10.1073/pnas.1613345114. [PubMed: 28760957]

11. DeVience SJ, Lu X, Proctor J, Rangghran P, Melhem ER, Gullapalli R, Fiskum GM, Mayer D. Metabolic imaging of energy metabolism in traumatic brain injury using hyperpolarized [1–13C]pyruvate. Sci Rep 2017;7:1907. doi: 10.1038/s41598-017-01736-x. [PubMed: 28507314]
12. Mayer D, Yen Y-F, Takahashi A, Josan S, Tropp J, Rutt BK, Hurd RE, Spielman DM, Pfefferbaum A. Dynamic and high-resolution metabolic imaging of hyperpolarized [1–13C]-pyruvate in the rat brain using a high-performance gradient insert. Magn Reson Med 2011;65:1228–1233. doi: 10.1002/mrm.22707. [PubMed: 21500253]
13. Park JM, Recht LD, Josan S, Merchant M, Jang T, Yen Y-F, Hurd RE, Spielman DM, Mayer D. Metabolic response of glioma to dichloroacetate measured in vivo by hyperpolarized (13)C magnetic resonance spectroscopic imaging. Neuro-oncology 2013;15:433–441. doi: 10.1093/neuonc/nos319. [PubMed: 23328814]
14. Erakovic V, Zupan G, Varljen J, Laginja J, Simonic A. Altered activities of rat brain metabolic enzymes in electroconvulsive shock-induced seizures. Epilepsia 2001;42:181–189. [PubMed: 11240587]
15. Nelson SJ, Kurhanewicz J, Vigneron DB, et al. Metabolic imaging of patients with prostate cancer using hyperpolarized [1-^{13}C]pyruvate. Sci Transl Med 2013;5:198ra108. doi: 10.1126/scitranslmed.3006070.
16. Grist JT, McLean MA, Riemer F, et al. Quantifying normal human brain metabolism using hyperpolarized [1–13C]pyruvate and magnetic resonance imaging. Neuroimage 2019;189:171–179. doi: 10.1016/j.neuroimage.2019.01.027. [PubMed: 30639333]
17. Lee CY, Soliman H, Geraghty BJ, Chen AP, Connelly KA, Endre R, Perks WJ, Heyn C, Black SE, Cunningham CH. Lactate topography of the human brain using hyperpolarized 13C-MRI. Neuroimage 2019;204:116202. doi: 10.1016/j.neuroimage.2019.116202. [PubMed: 31557546]
18. Park I, Larson PEZ, Gordon JW, et al. Development of methods and feasibility of using hyperpolarized carbon-13 imaging data for evaluating brain metabolism in patient studies. Magn Reson Med 2018;80:864–873. doi: 10.1002/mrm.27077. [PubMed: 29322616]
19. Miloushev VZ, Granlund KL, Boltyanskiy R, et al. Metabolic Imaging of the Human Brain with Hyperpolarized 13C Pyruvate Demonstrates 13C Lactate Production in Brain Tumor Patients. Cancer Res. 2018;78:3755–3760. doi: 10.1158/0008-5472.CAN-18-0221. [PubMed: 29769199]
20. Chen J, Patel TR, Pinho MC, et al. Preoperative imaging of glioblastoma patients using hyperpolarized 13C pyruvate. Neuro-Oncol Adv. 2021;3:vdab092. doi:10.1093/noajnl/vdab092.
21. Hackett EP, Pinho MC, Harrison CE, et al. Imaging Acute Metabolic Changes in Patients with Mild Traumatic Brain Injury Using Hyperpolarized [1–13C]Pyruvate. iScience 2020;23:101885. doi: 10.1016/j.isci.2020.101885. [PubMed: 33344923]
22. Gordon JW, Chen H-Y, Autry A, et al. Translation of Carbon-13 EPI for hyperpolarized MR molecular imaging of prostate and brain cancer patients. Magn Reson Med 2019;81:2702–2709. doi: 10.1002/mrm.27549. [PubMed: 30375043]
23. Mammoli D, Gordon J, Autry A, et al. Kinetic Modeling of Hyperpolarized Carbon-13 Pyruvate Metabolism in the Human Brain. IEEE Trans Med Imaging 2020;39:320–327. doi: 10.1109/TMI.2019.2926437. [PubMed: 31283497]
24. Ma J, Hashoian RS, Sun C, Wright SM, Ivanishev A, Lenkinski RE, Malloy CR, Chen AP, Park JM. Development of 1H/13C RF head coil for hyperpolarized 13C imaging of human brain. In: Montreal, Canada; 2019. #568.
25. Chen J, Hackett EP, Kovacs Z, Malloy CR, Park JM. Assessment of hepatic pyruvate carboxylase activity using hyperpolarized [1–13 C]-l-lactate. Magn Reson Med 2021;85:1175–1182. doi: 10.1002/mrm.28489. [PubMed: 32936474]
26. Park JM, Josan S, Jang T, Merchant M, Yen Y-F, Hurd RE, Recht L, Spielman DM, Mayer D. Metabolite kinetics in C6 rat glioma model using magnetic resonance spectroscopic imaging of hyperpolarized [1-(13)C]pyruvate. Magn Reson Med 2012;68:1886–1893. doi: 10.1002/mrm.24181. [PubMed: 22334279]
27. Schroeder MA, Ali MA, Hulikova A, Supuran CT, Clarke K, Vaughan-Jones RD, Tyler DJ, Swietach P. Extramitochondrial domain rich in carbonic anhydrase activity improves myocardial energetics. Proc Natl Acad Sci USA 2013;110:E958–67. doi: 10.1073/pnas.1213471110. [PubMed: 23431149]

28. Schroeder MA, Lau AZ, Chen AP, et al. Hyperpolarized (13)C magnetic resonance reveals early- and late-onset changes to in vivo pyruvate metabolism in the failing heart. Eur. J. Heart Fail 2013;15:130–140. doi: 10.1093/eurjhf/hfs192. [PubMed: 23258802]
29. Park JM, Josan S, Mayer D, Hurd RE, Chung Y, Bendahan D, Spielman DM, Jue T. Hyperpolarized 13C NMR observation of lactate kinetics in skeletal muscle. J Exp Biol 2015;218:3308–3318. doi: 10.1242/jeb.123141. [PubMed: 26347554]
30. Smith SM. Fast robust automated brain extraction. Hum Brain Mapp 2002;17:143–155. doi: 10.1002/hbm.10062. [PubMed: 12391568]
31. Zhang Y, Brady M, Smith S. Segmentation of brain MR images through a hidden Markov random field model and the expectation-maximization algorithm. IEEE Trans Med Imaging 2001;20:45–57. doi: 10.1109/42.906424. [PubMed: 11293691]
32. Bergersen LH. Lactate transport and signaling in the brain: potential therapeutic targets and roles in body-brain interaction. J Cereb Blood Flow Metab 2015;35:176–185. doi: 10.1038/jcbfm.2014.206. [PubMed: 25425080]
33. Froberg MK, Gerhart DZ, Enerson BE, Manivel C, Guzman-Paz M, Seacotte N, Drewes LR. Expression of monocarboxylate transporter MCT1 in normal and neoplastic human CNS tissues. Neuroreport 2001;12:761–765. doi: 10.1097/00001756-200103260-00030. [PubMed: 11277580]
34. Harris T, Eliyahu G, Frydman L, Degani H. Kinetics of hyperpolarized 13C1-pyruvate transport and metabolism in living human breast cancer cells. Proc Natl Acad Sci USA 2009;106:18131–18136. doi: 10.1073/pnas.0909049106. [PubMed: 19826085]
35. Rao Y, Gammon S, Zacharias NM, Liu T, Salzillo T, Xi Y, Wang J, Bhattacharya P, Piwnica-Worms D. Hyperpolarized [1–13C]pyruvate-to-[1–13C]lactate conversion is rate-limited by monocarboxylate transporter-1 in the plasma membrane. Proc Natl Acad Sci USA 2020;117:22378–22389. doi: 10.1073/pnas.2003537117. [PubMed: 32839325]
36. Hackett EP, Shah BR, Cheng B, et al. Probing Cerebral Metabolism with Hyperpolarized 13C Imaging after Opening the Blood-Brain Barrier with Focused Ultrasound. ACS Chem Neurosci 2021;12:2820–2828. doi: 10.1021/acschemneuro.1c00197. [PubMed: 34291630]
37. Hurd RE, Yen Y-F, Mayer D, et al. Metabolic imaging in the anesthetized rat brain using hyperpolarized [1–13C] pyruvate and [1–13C] ethyl pyruvate. Magn Reson Med 2010;63:1137–1143. doi: 10.1002/mrm.22364. [PubMed: 20432284]
38. Miller JJ, Grist JT, Serres S, et al. 13C Pyruvate Transport Across the Blood-Brain Barrier in Preclinical Hyperpolarised MRI. Sci Rep 2018;8:15082. doi: 10.1038/s41598-018-33363-5. [PubMed: 30305655]
39. Pérez-Escuredo J, Van Hée VF, Sboarina M, Falces J, Payen VL, Pellerin L, Sonveaux P. Monocarboxylate transporters in the brain and in cancer. Biochim Biophys Acta 2016;1863:2481–2497. doi: 10.1016/j.bbamcr.2016.03.013. [PubMed: 26993058]
40. Li X, Sarkar SN, Purdy DE, Briggs RW. Quantifying cerebellum grey matter and white matter perfusion using pulsed arterial spin labeling. Biomed Res Int 2014;2014:108691–12. doi: 10.1155/2014/108691. [PubMed: 24949416]
41. Chandler WL, Fine JS, Emery M, Weaver D, Reichenbach D, Clayson KJ. Regional creatine kinase, adenylate kinase, and lactate dehydrogenase in normal canine brain. Stroke 1988;19:251–255. doi: 10.1161/01.str.19.2.251. [PubMed: 2830684]
42. Leen WG, Willemsen MA, Wevers RA, Verbeek MM. Cerebrospinal fluid glucose and lactate: age-specific reference values and implications for clinical practice. Mendelson JE, editor. PLoS ONE 2012;7:e42745. doi: 10.1371/journal.pone.0042745. [PubMed: 22880096]
43. Prichard J, Rothman D, Novotny E, Petroff O, Kuwabara T, Avison M, Howseman A, Hanstock C, Shulman R. Lactate rise detected by 1H NMR in human visual cortex during physiologic stimulation. Proc. Natl. Acad. Sci. U.S.A 1991;88:5829–5831. doi: 10.1073/pnas.88.13.5829. [PubMed: 2062861]
44. Bélanger M, Allaman I, Magistretti PJ. Brain energy metabolism: focus on astrocyte-neuron metabolic cooperation. Cell Metab. 2011;14:724–738. doi: 10.1016/j.cmet.2011.08.016. [PubMed: 22152301]
45. Xu T, Mayer D, Gu M, Yen Y-F, Josan S, Tropp J, Pfefferbaum A, Hurd R, Spielman D. Quantification of in vivo metabolic kinetics of hyperpolarized pyruvate in rat kidneys using

dynamic 13C MRSI. NMR Biomed 2011;24:997–1005. doi: 10.1002/nbm.1719. [PubMed: 21538639]

46. Wespi P, Steinhauser J, Kwiatkowski G, Kozerke S. Overestimation of cardiac lactate production caused by liver metabolism of hyperpolarized [1–13 C]pyruvate. Magn Reson Med 2018;80:1882–1890. doi: 10.1002/mrm.27197. [PubMed: 29607535]
47. Yu AC, Drejer J, Hertz L, Schousboe A. Pyruvate carboxylase activity in primary cultures of astrocytes and neurons. J Neurochem 1983;41:1484–1487. [PubMed: 6619879]
48. Shank RP, Bennett GS, Freytag SO, Campbell GL. Pyruvate carboxylase: an astrocyte-specific enzyme implicated in the replenishment of amino acid neurotransmitter pools. Brain Res. 1985;329:364–367. doi: 10.1016/0006-8993(85)90552-9. [PubMed: 3884090]
49. Lee P, Leong W, Tan T, Lim M, Han W, Radda GK. In vivo hyperpolarized carbon-13 magnetic resonance spectroscopy reveals increased pyruvate carboxylase flux in an insulin-resistant mouse model. Hepatology 2013;57:515–524. doi: 10.1002/hep.26028. [PubMed: 22911492]
50. Merritt ME, Harrison C, Sherry AD, Malloy CR, Burgess SC. Flux through hepatic pyruvate carboxylase and phosphoenolpyruvate carboxykinase detected by hyperpolarized 13C magnetic resonance. 2011;108:19084–19089. doi: 10.1073/pnas.1111247108.
51. Waagepetersen HS, Qu H, Schousboe A, Sonnewald U. Elucidation of the quantitative significance of pyruvate carboxylation in cultured cerebellar neurons and astrocytes. J. Neurosci. Res 2001;66:763–770. doi: 10.1002/jnr.10061. [PubMed: 11746400]
52. Sonnewald U, Rae C. Pyruvate carboxylation in different model systems studied by (13)C MRS. Neurochem. Res 2010;35:1916–1921. doi: 10.1007/s11064-010-0257-5. [PubMed: 20842423]
53. Waagepetersen HS, Sonnewald U, Larsson OM, Schousboe A. A possible role of alanine for ammonia transfer between astrocytes and glutamatergic neurons. J Neurochem 2000;75:471–479. doi: 10.1046/j.1471-4159.2000.0750471.x. [PubMed: 10899921]
54. Park JM, Spielman DM, Josan S, Jang T, Merchant M, Hurd RE, Mayer D, Recht LD. Hyperpolarized (13) C-lactate to (13) C-bicarbonate ratio as a biomarker for monitoring the acute response of anti-vascular endothelial growth factor (anti-VEGF) treatment. NMR Biomed 2016;29:650–659. doi: 10.1002/nbm.3509. [PubMed: 26990457]
55. Gordon JW, Hansen RB, Shin PJ, Feng Y, Vigneron DB, Larson PEZ. 3D hyperpolarized C-13 EPI with calibrationless parallel imaging. J. Magn. Reson 2018;289:92–99. doi: 10.1016/j.jmr.2018.02.011. [PubMed: 29476930]
56. Dominguez-Viqueira W, Geraghty BJ, Lau JYC, Robb FJ, Chen AP, Cunningham CH. Intensity correction for multichannel hyperpolarized 13C imaging of the heart. Magn Reson Med 2016;75:859–865. doi: 10.1002/mrm.26042. [PubMed: 26619820]
57. Park JM, Reed GD, Liticker J, et al. Effect of Doxorubicin on Myocardial Bicarbonate Production from Pyruvate Dehydrogenase in Women with Breast Cancer. Circ. Res 2020;104:19773. doi: 10.1161/CIRCRESAHA.120.317970.

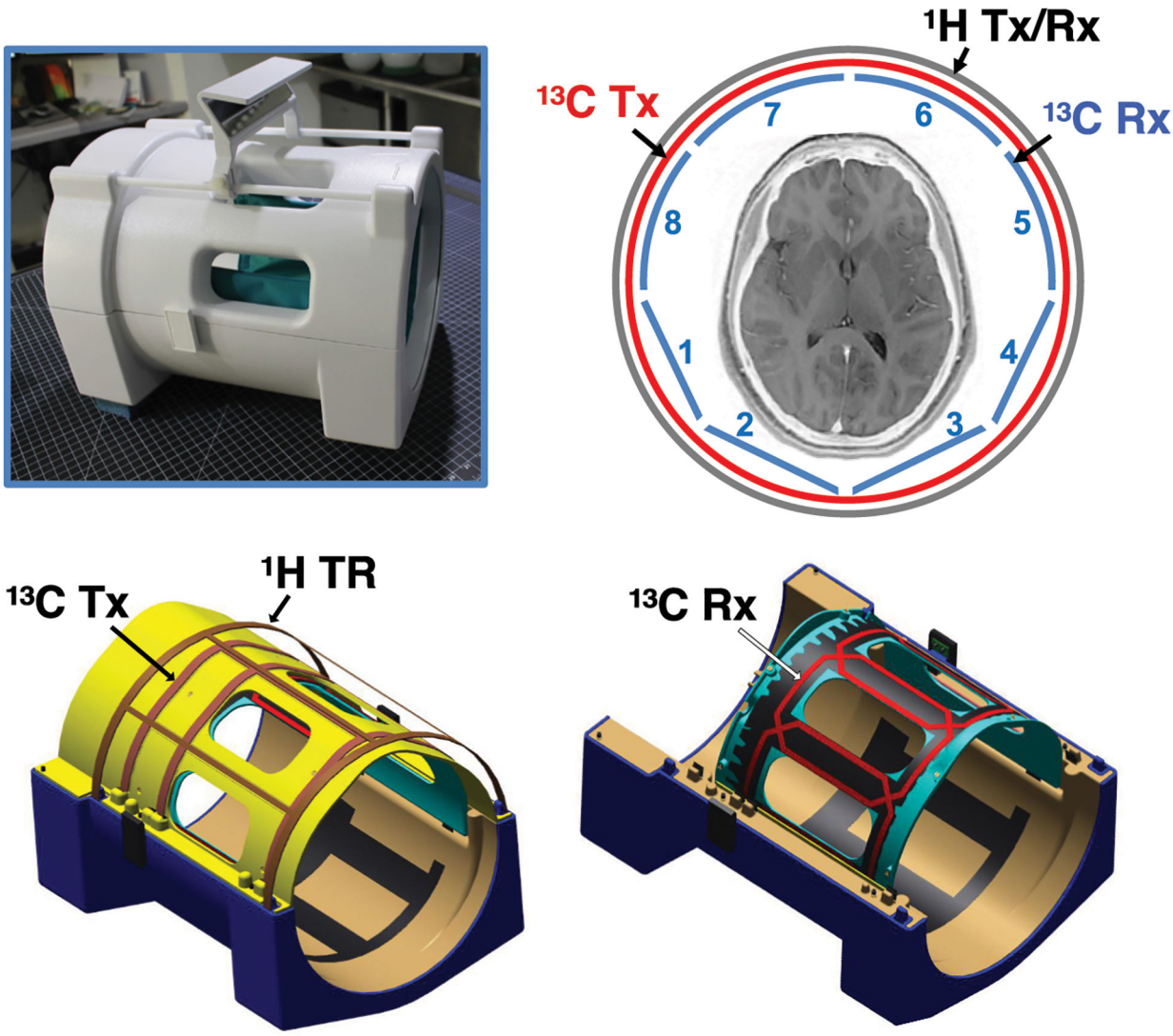

Figure 1. $^{13}C/^{1}H$ dual-frequency RF head coil.

The $^{13}C/^{1}H$ dual-frequency RF head coil that consists of ^{1}H quadrature Tx and Rx, ^{13}C quadrature Tx and 8-channel ^{13}C receive Rx arrays was developed for this study.

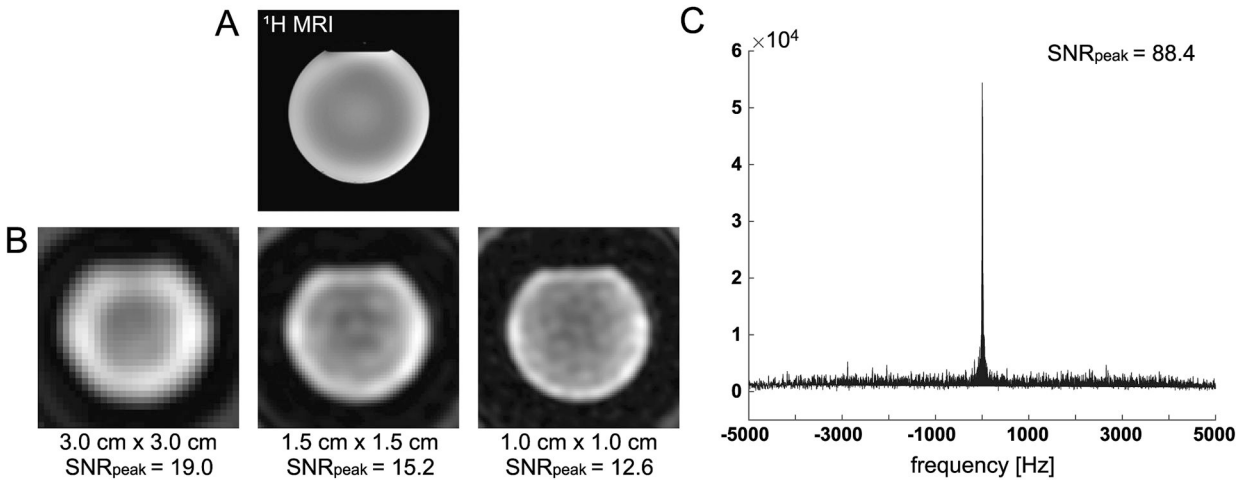

Figure 2. SNR comparison between ^{13}C MRS with small flip-angle excitation and ^{13}C MRI with 90° excitation.

(A) ^{1}H T_2-weighted fast spin echo image of the gadolinium-doped spherical [^{13}C]HCO_3^- phantom was acquired with the ^{13}C/^{1}H dual-frequency RF head coil. (B) ^{13}C images of the phantom with three nominal in-plane spatial resolutions (3.0 cm × 3.0 cm, 1.5 cm × 1.5 cm and 1.0 cm × 1.0 cm) were acquired using a 2D slice-selective spiral imaging sequence with 90° excitation. (C) ^{13}C spectrum acquired using MRS with 6.5° flip-angle from the same phantom.

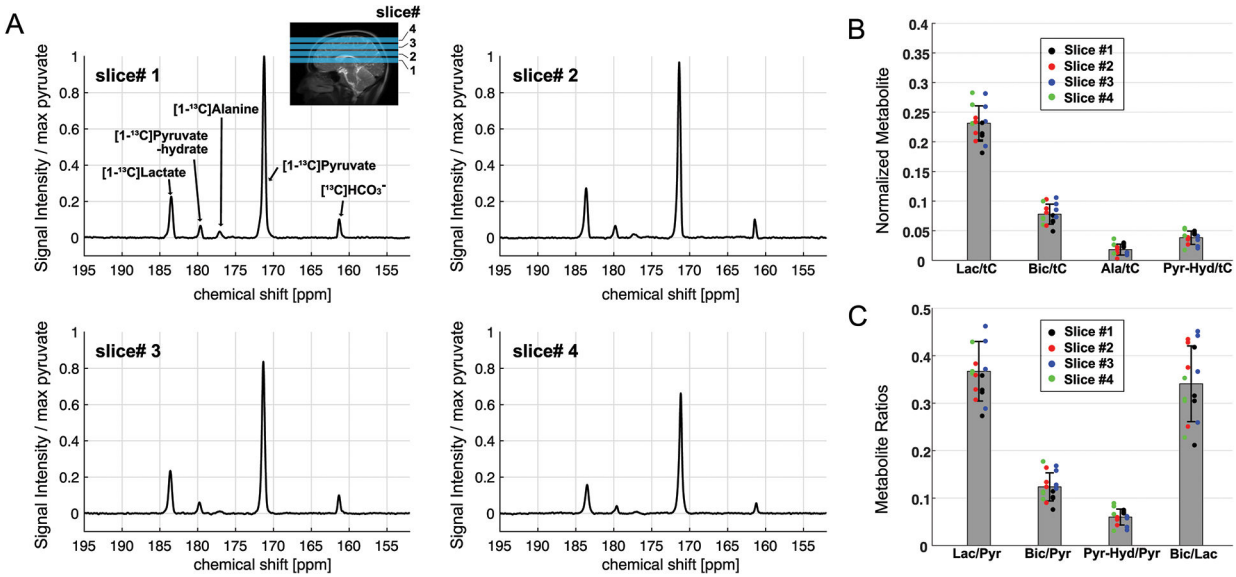

Figure 3. Time-averaged ^{13}C spectra of four axial brain slices.

(A) Time-averaged, coil-combined, and phase-corrected spectra, normalized by the maximum pyruvate peak, from a representative participant. Prescription of four axial slices for HP ^{13}C MRS is shown in the sagittal ^{1}H MRI. (B) HP [1-^{13}C]lactate, [^{13}C]HCO_3^-, [1-^{13}C]alanine, and [1-^{13}C]pyruvate-hydrate, normalized by total HP ^{13}C (tC). Measurement from slice #1, #2, #3 and #4 are color-coded in black, red, blue, and green, respectively. (C) Metabolite ratios of lactate-to-pyruvate, HCO_3^--to-pyruvate, pyruvate-hydrate-to-pyruvate, and HCO_3^--to-lactate.

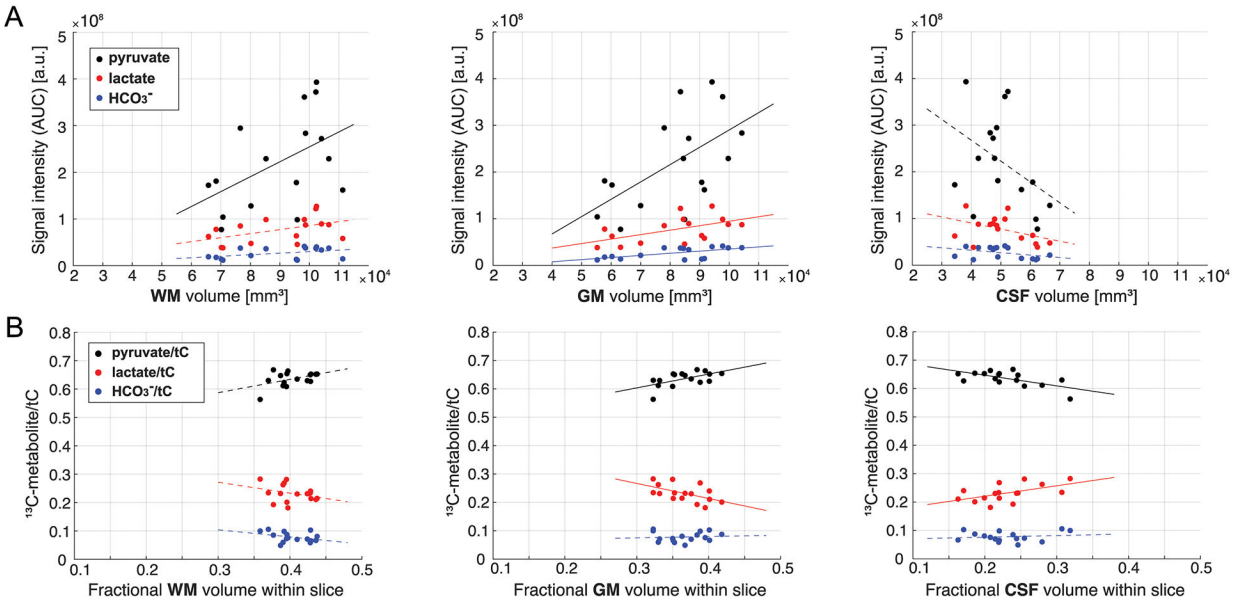

Figure 4. Correlation of HP signals to brain volumes.

(A) Area under the curves (AUCs) for HP [1-^{13}C]pyruvate (black dots), [1-^{13}C]lactate (red dots), and [^{13}C]HCO_3^- (blue dots) from each brain slice in relation to the brain volumes of WM, GM, and CSF within the slice. (B) HP ^{13}C signal intensities of each metabolite relative to the total HP ^{13}C signal (tC) within the slice in relation to fractional brain volumes of WM, GM, and CSF of the slice. Lines indicate linear regressions (solid: p-value ≤ 0.05, dotted: p > 0.5). Lac: [1-^{13}C]lactate, Bic: [^{13}C]HCO_3^-, Ala: [1-^{13}C]alanine, Pyr-Hyd: [1-^{13}C]pyruvate hydrate, Pyr: [1-^{13}C]pyruvate, WM: white matter, GM: grey matter, CSF: cerebrospinal fluid.

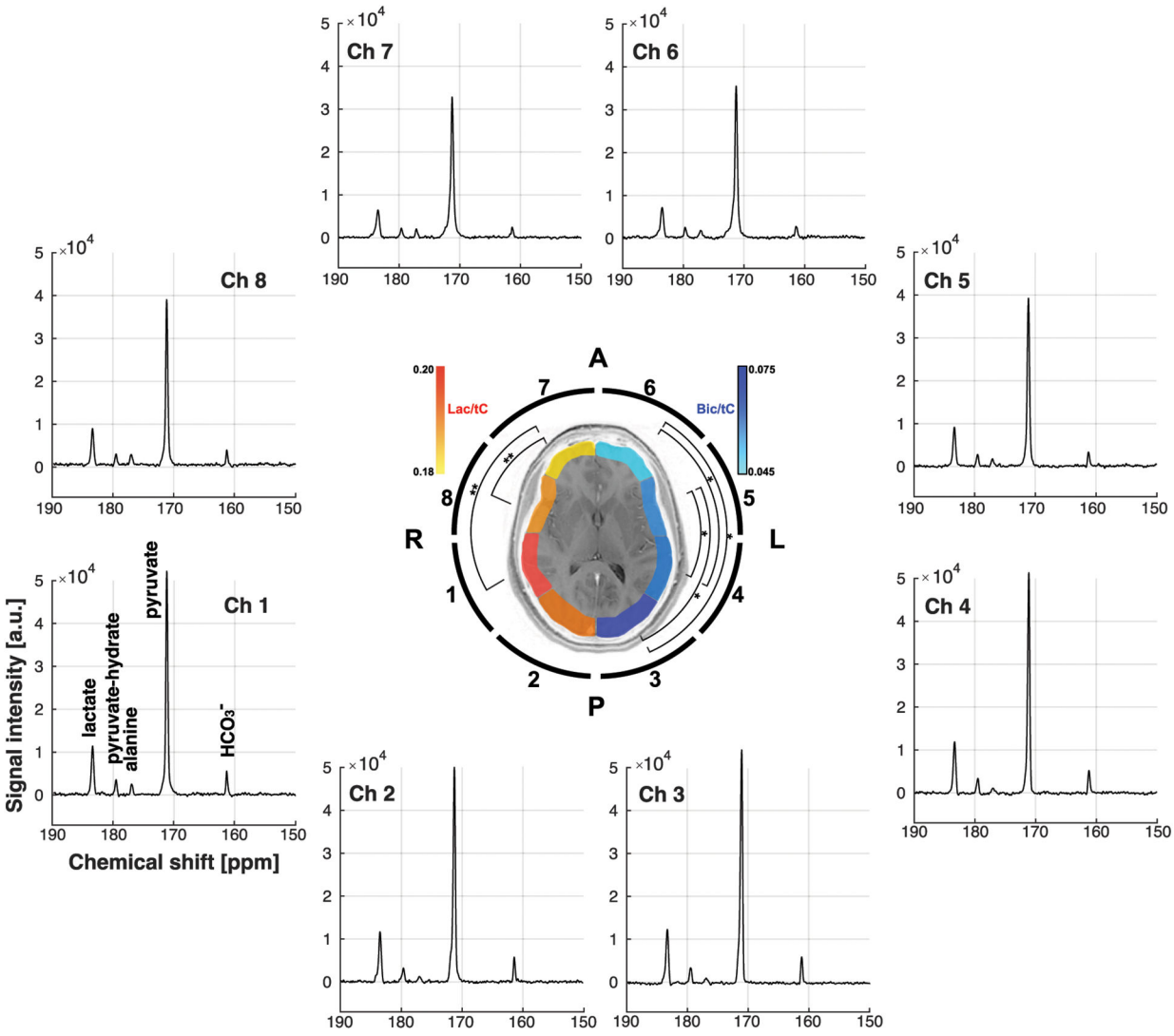

Figure 5. Coil-wise reconstruction of HP ^{13}C spectra.

Time-averaged ^{13}C spectra and metabolite ratios for individual ^{13}C coil elements. [1-^{13}C]Lactate and [^{13}C]HCO_3^-, normalized by total HP ^{13}C signals (tC), from each ^{13}C channel are color-coded in red and blue, respectively, and overlaid on the corresponding brain slice (slice #1) to indicate the region-weighted measurements.

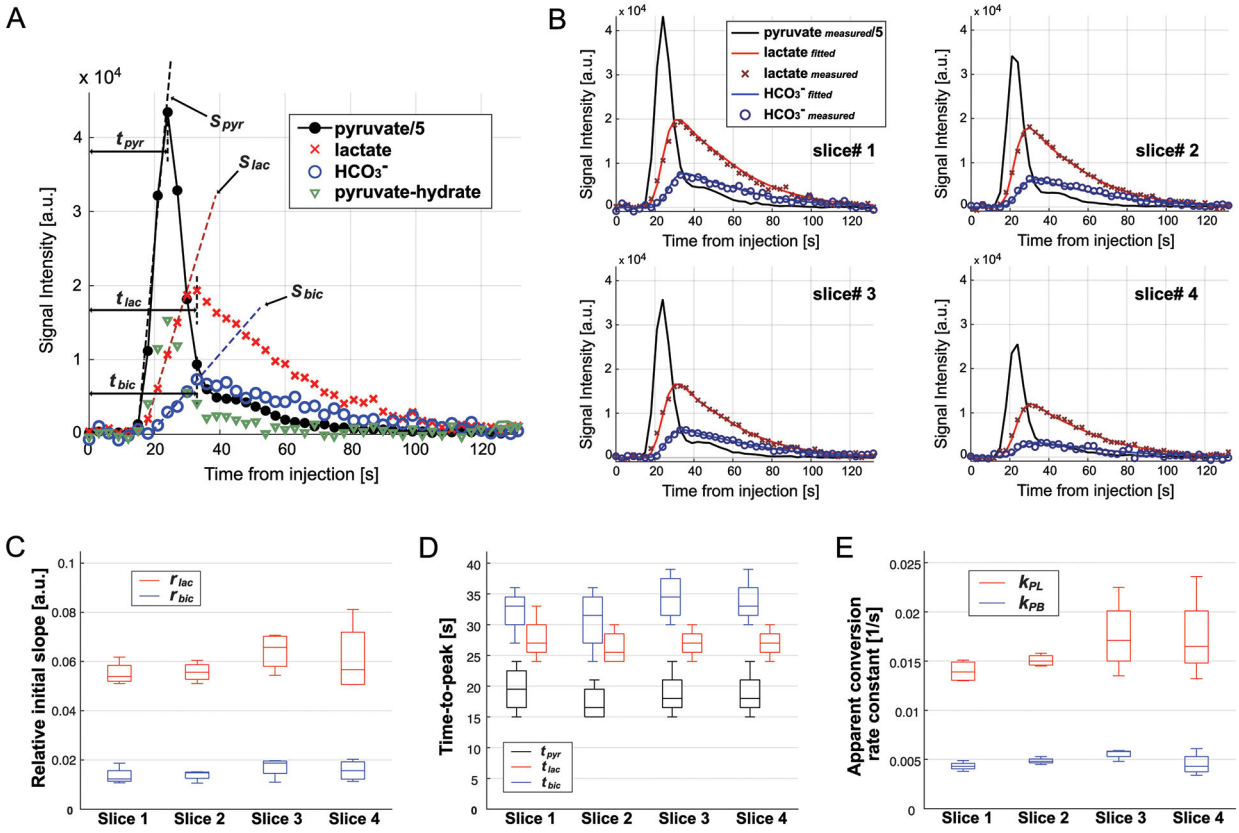

Figure 6. Kinetic analysis.

(A) Representative time-curves of HP [1-^{13}C]pyruvate (black filled circle), [1-^{13}C]lactate (red cross), [^{13}C]HCO_3^- (blue empty circle), and [1-^{13}C]pyruvate-hydrate (green triangle). Times-to-peak and initial slope for pyruvate, lactate, and HCO_3^- are shown. (B) Measured (markers) and fitted (solid lines) for [1-^{13}C]lactate (red) and [^{13}C]HCO_3^- (blue) in slices #1 – #4 from a representative participant. Measured [1-^{13}C]pyruvate is shown in black. (C) Initial slopes of [1-^{13}C]lactate (red) and [^{13}C]HCO_3^- (blue) relative to the initial slope of [1-^{13}C]pyruvate, (D) times-to-peak for [1-^{13}C]pyruvate (black), [1-^{13}C]lactate (red), and [^{13}C]HCO_3^- (blue) from the start of HP [1-^{13}C]pyruvate injection, and (E) apparent conversion rate constants from [1-^{13}C]pyruvate to [1-^{13}C]lactate (k_{PL}, red) and to [^{13}C]HCO_3^- (k_{PB}, blue) for each brain slice.

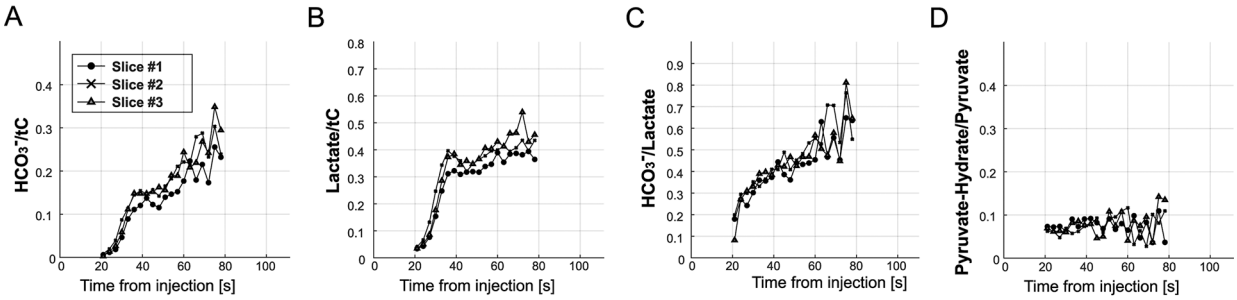

Figure 7. Time-resolved metabolic ratios.

(A) HCO_3^-/tC, (B) lactate/tC and (C) HCO_3^-/lactate increased over time after each HP injection while (D) pyruvate-hydrate/pyruvate was maintained constant. The increasing behavior of these metabolite ratios was consistent over different brain slices.

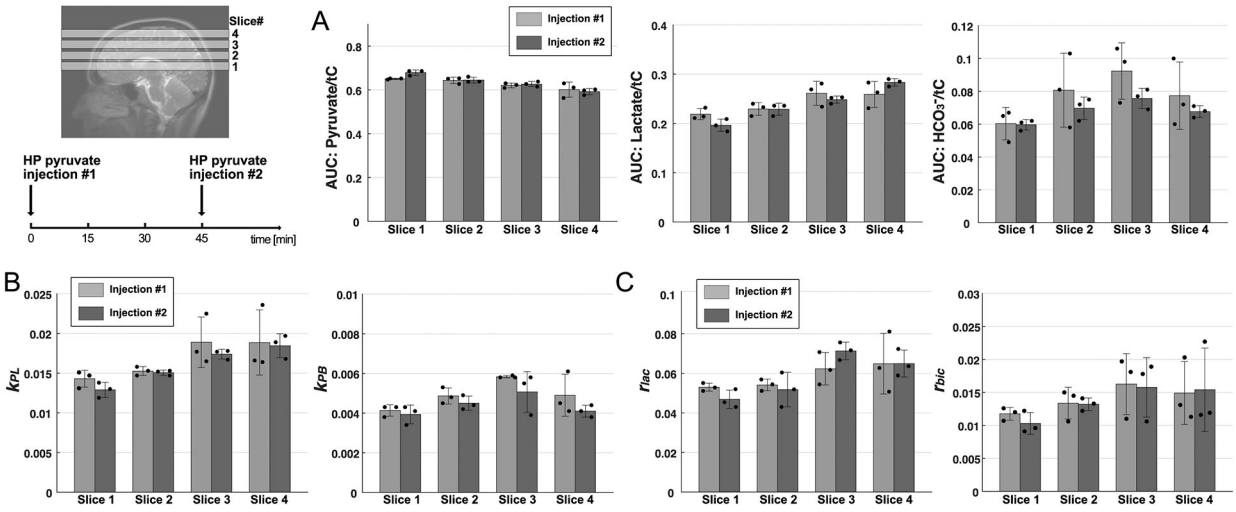

Figure 8. Reproducibility of HP [1-^{13}C]pyruvate.

(A) Area under the curves (AUCs) for pyruvate, lactate, and bicarbonate, normalized by total HP ^{13}C signals (tC), (B) apparent pyruvate conversion rate constants to lactate (k_{PL}) and bicarbonate (k_{PB}), and (C) initial slopes of lactate and bicarbonate production relative to the pyruvate slope were comparable between two consecutive HP [1-^{13}C]pyruvate studies. The two HP pyruvate MRS data were acquired with a 45-min interval between the injections.

Table 1.

Study participant demographics.

Participant ID	1	2	3	4
Age (years)	25	48	24	65
Gender	M	F	F	F
BMI (kg/m^2)	29.0	26.4	22.3	27.8
#Injections	1	2	2	2

Table 2.

Metabolite ratios of HP ^{13}C signals in the brain.

	Slice 1	Slice 2	Slice 3	Slice 4
Lactate/tC	0.212 ± 0.018	0.222 ± 0.018	0.244 ± 0.040	0.242 ± 0.039
Bicarbonate/tC	0.065 ± 0.012	0.082 ± 0.019	0.091 ± 0.014	0.073 ± 0.019
Alanine/tC	0.026 ± 0.004	0.014 ± 0.008	0.011 ± 0.002	0.0021 ± 0.013
Bicarbonate/Lactate	0.313 ± 0.085	0.373 ± 0.086	0.381 ± 0.089	0.299 ± 0.052
Pyruvate-Hydrate/Pyruvate	0.055 ± 0.003	0.054 ± 0.008	0.048 ± 0.014	0.067 ± 0.026